Contents list available at CBIORE journal website

International Journal of Renewable Energy Development

Journal homepage: https://ijred.cbiore.id

Research Article

Upcycling EAF graphite electrode waste into graphene-oxide–doped PEDOT:PSS for inverted perovskite solar cells

Yus Rama Denny[a,b*], Mohamad Fadli[c], Muhammad Iman Santoso[d], Sulaeman Deni Ramdani[e], Rafa Jafar[f], Meilani[f]

[a]*Department of Physics Education, University of Sultan Ageng Tirtayasa, Banten, Indonesia*

[b]*Photovoltaic, Functional Device, and Artificial Intelligence Laboratory, University of Sultan Ageng Tirtayasa, Banten, Indonesia*

[c]*Department of Metallurgical Engineering, University of Sultan Ageng Tirtayasa, Banten, Indonesia*

[d]*Department of Informatics Engineering, University of Sultan Ageng Tirtayasa, Banten, Indonesia*

[e]*Department of Vocational Mechanical Engineering, University of Sultan Ageng Tirtayasa, Banten, Indonesia*

[f]*PT Daur Ulang Sampah Elektronik (EwasteRJ), Jakarta, Indonesia*

Abstract. Poly(3,4-ethylenedioxythiophene):polystyrene sulfonate (PEDOT:PSS) is widely used as a hole-transport layer (HTL) in inverted perovskite solar cells (PSCs), but its acidity and moisture affinity can limit device performance. This study aimed to evaluate a circular-materials route by upcycling electric-arc-furnace (EAF) graphite-electrode waste into graphene oxide (GO) and applying GO-doped PEDOT:PSS as an HTL modifier, while identifying a practical low-temperature processing window for inverted PSCs under ambient conditions. Graphene oxide was synthesized from EAF graphite waste and dispersed in water (1 mg mL^{-1}), then blended with PEDOT:PSS at different loadings. Inverted PSCs with an ITO/GO-doped PEDOT:PSS/$CH_3NH_3PbI_{3-x}Cl_x$/PCBM/Ag architecture were fabricated in ambient laboratory air (25–27 °C; RH ≈ 40%) without a glovebox. The effects of GO loading and perovskite annealing temperature (70–130 °C) were evaluated using J–V measurements under AM1.5G illumination, supported by SEM and XRD analyses. Moderate GO addition was associated with improved film coverage and fewer pinholes, while XRD indicated better phase formation near 100 °C. In contrast, excessive annealing (≈130 °C) increased PbI_2 signatures and coincided with severe performance degradation. The optimum condition (600 µL GO per 1 mL PEDOT:PSS and 100 °C annealing) produced a champion power conversion efficiency of 0.80%, with VOC = 0.795 V, JSC = 3.48 mA cm^{-2}, and FF = 28.9%. Although the efficiency remained modest, the results demonstrated the feasibility of waste-derived GO as a functional PEDOT:PSS interfacial modifier and established a low-temperature processing window governing film integrity and degradation signatures in inverted PSCs, providing a basis for further optimization.

Keywords: perovskite solar cells; hole transport layer; electric arc furnace, graphene oxide, PEDOT:PSS.

@ The author(s). Published by CBIORE. This is an open access article under the CC BY-SA license (http://creativecommons.org/licenses/by-sa/4.0/).

Received: 25th Nov 2025; Revised: 15th January 2026; Accepted: 26th Feb 2026; Available online: 7th March 2026

1. Introduction

Solar cells, also known as photovoltaic (PV) cells, are technologies that can convert solar energy from photons into electrical energy. The development of solar cells has reached the third generation, namely, perovskite solar cells, which are the evolution of dye-sensitized solar cells (DSSC) (Hussain *et al.*, 2018). One of the essential parts of perovskite solar cells is the hole transport material (HTM). Inverted PSCs (p-i-n) are attractive for low-temperature processing and flexible substrates; however, the conventional HTL, PEDOT:PSS, is acidic and hygroscopic, offers limited electron-blocking ability, and can induce interfacial instability, thereby motivating interface engineering (Yang *et al.*, 2022). The HTM needs to be optimized to allow the photon-generated carriers in the active perovskite layer to transport into the electrode. An effective HTM must have a suitable energy level with the perovskite layer, sufficient electrical conductivity, high optical transparency, and good chemical stability (Niu *et al.*, 2017). The HTM commonly used in inverted perovskite solar cells is Poly(3,4-ethylenedioxythiophene) polystyrene sulfonate (PEDOT:PSS) (Han *et al.*, 2020). However, the high acidity of the PEDOT:PSS solution can damage the ITO and perovskite layers, which limits the stability and performance of perovskite solar cells (Yu *et al.*, 2018). Therefore, modifying the PEDOT:PSS layer is necessary to obtain the abovementioned HTM criteria with graphene oxide (GO) doping. GO loading in PEDOT:PSS has been reported to influence HTL surface properties and interfacial energetics. In some studies, moderate GO loading is associated with lower contact angle and more uniform perovskite nucleation/coverage, which can be accompanied by improved Voc/FF, whereas excessive GO increases HTL sheet resistance and may reduce transmittance, leading to a trade-off in device performance (Nguyen *et al.*, 2022).

Graphene oxide (GO) is a graphene sheet functionalized with oxygen-containing functional groups in the form of epoxy, hydroxyl, and various other groups (Luo *et al.*, 2017). Graphene oxide has been proven to be used as HTM in perovskite solar

* Corresponding author
Email: yusramadenny@untirta.ac.id (Y. R. Denny)

https://doi.org/10.61435/ijred.2026.62013
ISSN: 2252-4940/© 20xx.The Author(s). Published by CBIORE

cells (PSCs) and produces a PCE of 12.4%. However, the lack of conductivity of GO due to its high oxygen content makes the performance of the PSCs very sensitive to the GO layer thickness (Wu *et al*., 2014). The use of GO-doped PEDOT:PSS solution as HTM has been done by Niu et al. (Niu *et al*., 2017). PSCs with HTM in the form of 500 µl GO-doped PEDOT:PSS produced 14.20% PCE, which is increased compared to the pristine PEDOT:PSS (11.99%). However, it is known that there is a decrease in the PCE value along with the increase in the amount of doped GO caused by the increase in HTM resistance (Niu *et al*., 2017). In addition, GO is also expected to increase the crystallinity of the perovskite layer because perovskite crystals tend to grow more easily on the GO layer than PEDOT:PSS (Yu *et al*., 2018). This is also influenced by the annealing temperature of the perovskite layer, where the higher the annealing temperature, the more perfect the perovskite crystal formation will be, thereby increasing the efficiency of the PSCs (Al-Mousoi *et al*., 2020).

Graphene oxide (GO) can be synthesized from graphite powder using the modified Hummers' method (Eluyemi *et al*., 2016). Graphite electrode waste from electric arc furnace (EAF) can replace synthetic graphite as a raw material for GO production because it has similar characteristics and specifications. In parallel, waste-derived carbons have emerged as sustainable feedstocks for PV: for instance, graphene nanosheets synthesized from waste cardboard have been demonstrated for perovskite solar cells, supporting the relevance of circular-materials approaches in HTL/interface engineering (Garg *et al*., 2024). Examination of the EAF graphite electrode by EDX followed by XRD revealed that the EAF graphite electrode contains 99.8% carbon, has a crystalline carbon structure, and has good conductivity (Sadeli *et al*., 2011). This graphite electrode waste can be obtained from smelting remnants in steel production in the EAF industry, which is no longer used (Insiyanda *et al*., 2019). By utilizing EAF graphite electrode waste, the cost for producing GO can be reduced, and environmental purposes, such as waste recycling, can be achieved.

GO-doped PEDOT:PSS as HTM is a fascinating concern to study because of its potential to increase the efficiency of perovskite solar cells. GO loading in PEDOT:PSS directly tunes the HTL surface energy and work function. Moderate GO reduces the contact angle and promotes uniform perovskite nucleation and coverage, thereby lowering interfacial recombination and improving VOC/FF (Al-Gamal *et al*., 2023; Nguyen *et al*., 2022). However, excessive GO increases HTL sheet resistance and can reduce optical transmittance, diminishing JSC and FF—hence a clear trade-off exists (Ali *et al*, 2022). In parallel, the perovskite annealing temperature governs intermediate-to-perovskite conversion, grain growth, and pinhole formation; performance typically follows an optimum window rather than a monotonic increase with temperature (Er-raji *et al*., 2023; Mateen *et al*., 2023; Wargulski *et al*., 2023). The studies on variations in the amount of doped GO in PEDOT:PSS and the annealed temperature of the perovskite layer need to be further investigated to obtain optimal variations, especially on the doped GO synthesized from EAF graphite electrode waste.

Therefore, this study was conducted to evaluate the feasibility of waste-derived GO (from EAF graphite-electrode waste) as a PEDOT:PSS modifier and to examine how GO loading and perovskite annealing temperature influence device behavior under practical ambient-air, low-temperature fabrication conditions. The goal is to identify a processing window and establish a circular-materials proof-of-concept, rather than to demonstrate state-of-the-art efficiency. The graphene oxide synthesis process was carried out using the modified Hummers' method, which was then dispersed in distilled water for further doping with PEDOT:PSS solution in varying amounts. The PSCs configuration was ITO/GO doped-PEDOT:PSS/$CH_3NH_3PbI_{3-x}Cl_x$/PCBM/Ag, and the efficiency is characterized by the solar cell IV test system.

The absolute device efficiencies in this study are modest, which we openly attribute to deliberately non-ideal, sustainability-oriented processing conditions. Specifically, devices were fabricated under ambient air rather than in a controlled glovebox, and the HTL modifier was derived from waste EAF graphite electrodes, introducing realistic variability in feedstock purity and processing. In addition, the process was intentionally constrained to low-temperature steps to maintain compatibility with energy-efficient manufacturing and potential flexible substrates. Within this context, the present work is positioned as a circular-materials and low-temperature proof-of-concept, demonstrating that waste-derived GO can functionally modify PEDOT:PSS and that a practical processing window exists (moderate GO loading and mild annealing) before thermal over-treatment induces PbI_2 signatures and performance collapse. Future optimization under tighter environmental control and expanded electrical diagnostics is expected to raise the absolute metrics while preserving the sustainability advantages.

2. Method

2.1 Graphene Oxide Synthesis

In this study, graphene oxide was synthesized from electric arc furnace (EAF) graphite electrode waste using the modified Hummers' method. EAF graphite electrode waste is reduced in size to −230 + 400 mesh (38–63 µm), using an ASTM E11/ISO 3310-1 sieve stack (openings: 63 µm top, 38 µm bottom), washed with ethanol and acetone in an ultrasonic bath, and dried in an oven. Three grams of graphite powder were put into 120 mL of a mixture of H_2SO_4 and H_3PO_4 solutions with a ratio of 9:1 in an Erlenmeyer flask. Then the mixture was stirred using a magnetic stirrer at a temperature of 100°C for 2 hours. The mixture was cooled to room temperature, then further cooled in an ice bath. After cooling, 15 g of KMnO4 was added to the mixture gradually during the first 1 hour of stirring, then stirring was continued for 1 hour to obtain a homogeneous mixture. The mixture was heated at 45°C, stirred for 1 hour, and then cooled to room temperature. A total of 250 mL of distilled water was added to the mixture slowly. At this stage, the color of the mixture changes from green to brownish-red. Furthermore, 20 ml of H_2O_2 was added until the color of the mixture changed to dark brown, indicating that graphite oxide had formed. The mixture is then allowed to stand for one night. Next, the precipitate in the mixture was filtered and redissolved in 250 mL of 10% HCl. The mixture was washed with distilled water until the pH was neutral. Then the precipitate was filtered and dried in an oven at a temperature of 100°C for 6 hours. The obtained graphene oxide was analyzed using a UV-Vis spectrophotometer (UH5300) and Raman spectroscopy (iHR320 Horiba).

2.2 Device Fabrication

The device fabrication and structure of the fabricated perovskite solar cell is an inverted planar (p-i-n planar) with ITO/GO – doped - PEDOT: PSS/$CH_3NH_3PbI_{3x}Cl_x$/PCBM/Ag

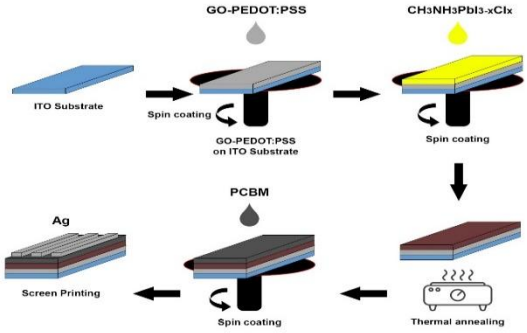

(a)

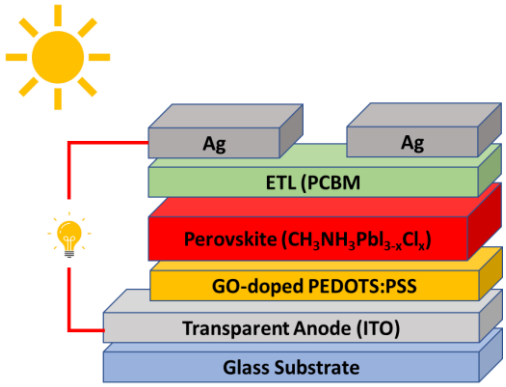

(b)

Fig. 1 Schematic of (a) device fabrication, and (b) Perovskite Solar Cell Structure.

configuration, as can be seen in Fig. 1(a, b). All device fabrication steps were performed under ambient laboratory air (T ≈ 25 °C; RH ≈ 40%) without a glovebox to assess process feasibility under practical conditions. Relative humidity was monitored using a digital hygrometer during coating and annealing.

2.3 ITO Substrate Cleaning

The ITO substrate was washed using detergent, distilled water, ethanol, acetone, and isopropyl alcohol in an ultrasonic bath for 10 minutes each, then exposed to UV light for 10 minutes. The clean ITO substrate was tested by a UV-Vis spectrophotometer (C-7000UV).

2.4 GO-Doped PEDOT:PSS Deposition

The PEDOT:PSS used in this work was HTL Solar PEDOT:PSS (Clevios™ HTL Solar, Ossila), with a reported solids content of 1.0–1.3 wt.% (manufacturer technical data). These values were used to convert volumetric GO additions into mass-based loading (mg mL^{-1} and wt% relative to PEDOT:PSS solids) for reproducibility.

Graphene oxide (GO) used in this study was synthesized in-house from EAF graphite-electrode waste and dispersed in distilled water at a concentration of 1 mg mL^{-1} using an ultrasonic bath for 30 min to prepare the GO stock dispersion. The GO stock was then mixed with 1 mL PEDOT:PSS (HTL Solar PEDOT:PSS, Clevios™ HTL Solar, Ossila; reported solids content 1.0–1.3 wt.%) at GO:PEDOT:PSS volume ratios of 0:1, 0.4:1, 0.6:1, and 0.8:1 mL, followed by ultrasonication for 30 min at room temperature to obtain homogeneous GO-doped PEDOT:PSS dispersions. Based on the GO stock concentration, these formulations correspond to 0, 0.4, 0.6, and 0.8 mg GO per 1 mL PEDOT:PSS, respectively. The equivalent GO concentrations in the final mixtures were 0, 0.286, 0.375, and 0.444 mg mL^{-1}, respectively.

For improved reproducibility, GO loading was also normalized as wt% relative to PEDOT:PSS solids. Using the manufacturer-reported PEDOT:PSS solids content (1.0–1.3 wt.%) and assuming a water-like dispersion density (~1 g mL^{-1}), the GO loadings for the 400, 600, and 800 µL formulations correspond approximately to 3.1–4.0 wt.%, 4.6–6.0 wt.%, and 6.2–8.0 wt.%, respectively. A volume of 30 µL of each GO-doped PEDOT:PSS dispersion was deposited onto the ITO substrate by spin coating at 6000 rpm for 30 s, followed by annealing at 120 °C for 15 min to form the HTL. The resulting ITO/GO-doped PEDOT:PSS films were characterized by UV–Vis spectroscopy using a C-7000UV spectrophotometer.

2.5 Perovskite ($CH_3NH_3PbI_{3-x}Cl_x$) Deposition

The perovskite ink precursor was heated at 70°C for 2 hours. 30 µl perovskite was deposited on the ITO/GO-doped-PEDOT:PSS substrate using a spin coating at a speed of 4000 rpm for 30 seconds in an environment with an RH of less than 40%. Subsequently, the substrate was annealed at temperatures varying from 70°C, 100°C, and 130°C for 25 minutes. The ITO/GO-doped-PEDOT:PSS/$CH_3NH_3PbI_{3-x}Cl_x$ devices were tested using a UV-Vis spectrophotometer (C-7000UV), X-Ray Diffraction (XRD) with a copper X-ray source (λ = 1.5406 Å), and Scanning Electron Microscopy (SEM).

2.6 PCBM and Ag Electrode Deposition

PCBM was prepared as much as 10 mg/ml in chlorobenzene and stirred for 6 hours. 20 µl PCBM was deposited on the ITO/GO-doped-PEDOT:PSS/$CH_3NH_3PbI_{3-x}Cl_x$ substrate using a spin coating at 1000 rpm for 30 seconds. The substrate was annealed at 80°C for 10 minutes, then tested using a UV-Vis spectrophotometer (C-7000UV). Next, the cathode strip was wiped with chlorobenzene. Finally, the silver conductive paste was deposited using a screen-printing method, then annealed at 120°C for 1 minute. The photovoltaic performance of the solar cells was measured in air without encapsulation using a solar cell I-V test system – automated (T2003) under AM 1.5G at 100 mW/cm^2 light illumination. The device architecture was defined using an Ossila 8-pixel multi-electrode mask (20 × 15 mm substrate format), which produces eight individual devices per substrate with an active area of 4 mm^2 (0.04 cm^2) per pixel. During J–V measurements, a shadow mask was used to maintain the same effective active area and minimize photocurrent overestimation.Rs and Rsh were obtained from local J–V slopes near V ≈ Voc and V ≈ 0, respectively. The sheet resistance of PEDOT:PSS and GO-doped PEDOT:PSS films deposited on glass/ITO was measured using a four-point probe as a function of GO loading and post-deposition annealing temperature (70, 100, and 130 °C) to evaluate conductivity changes in the HTL.

3. Results And Discussion

3.1 Graphene Oxide Characterizations

In order to investigate the optical property of graphene oxide, UV-Vis spectrophotometer was used to determine the characteristics of the absorbance vs wavelength. The UV-Vis spectra of graphene oxide are shown in Fig. 2a. Based on the spectra, the absorbance peak of the UV-Vis spectra of graphene oxide is known to be at a wavelength of 226 nm. This wavelength is close to the peak of the UV-Vis spectra of graphene oxide in a previous study conducted by Wazir and Kundi (2016), which is 230 nm. This value indicates a $\pi - \pi^*$ transition of the C–C aromatic bond (Wazir & Kundi, 2016).

Raman spectroscopy was carried out to analyze the level of defects and the characteristics of the graphene oxide layer formed using three types of reference peaks. The three peaks are the D-peak (defect) in the Raman shift of ~1350 cm$^{-1,}$ which indicates the level of material defect, the G-peak (graphitic) in the Raman shift of ~1600 cm$^{-1,}$ and the 2D-peak in the Raman shift of ~2700 cm^{-1}. The D peak indicates disturbances that may arise from certain defects such as vacancies, grain boundaries, and amorphous carbon species (Johra et al., 2014). The 2D peak indicates the number of graphene oxide layers formed.

The Raman shift and the intensity of the synthesized graphene oxide are presented in Fig. 2b. Based on the spectra, the D-peak was observed at a shift of 1350.26 cm^{-1} with an intensity of 713.316, while the G-peak was observed at a shift of 1599.09 cm^{-1} with an intensity of 779.851. The I_D/I_G ratio is known to be 0.91. This value indicates that the quality of the graphene oxide produced is quite good, with low defects.

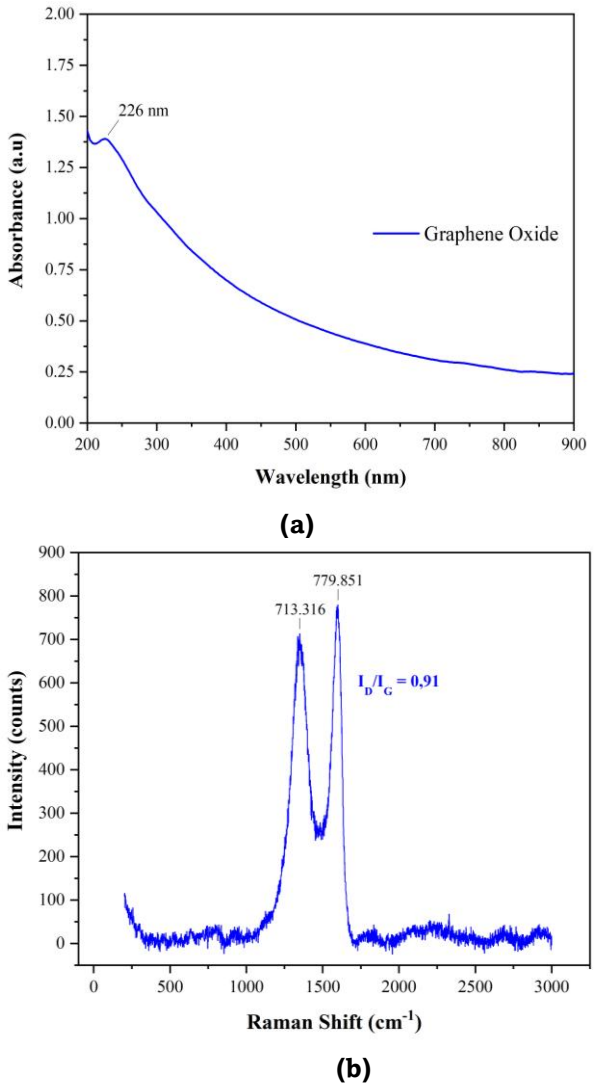

Fig. 2 (a) Graphene Oxide UV-Vis Spectra, and (b) Graphene Oxide Raman Spectra

However, in the Raman spectra, no 2D-peak was found. This shows that the graphene oxide layer formed is still quite a lot (multilayer). The peak location, intensity, and I_D/I_G ratio data are presented in Table 1.

3.2 Effect of Graphene Oxide Doping on Optical Properties

The ITO electrode and HTM must have a high transmittance to pass as much light or photons as possible into the perovskite layer. The transmittance spectra of ITO and ITO/PEDOT:PSS layers with variations in the amount of doped GO are presented in Fig. 3a. In these spectra, there was no significant change in the transmittance value from the addition of variations in the amount of doped GO in PEDOT:PSS. The transmittance values of these layers range from ~90% to ~98% in the visible light range, so that light can be transmitted well to

Table 1
Raman Peak Location, Intensity, and ID/IG Ratio of Graphene Oxide

Material	D-Peak		G-Peak		I_D/I_G
	Raman Shift (cm^{-1})	Intensity (counts)	Raman Shift (cm^{-1})	Raman Shift (cm^{-1})	
GO	1350.26	713.316	1599.09	779.851	0.91

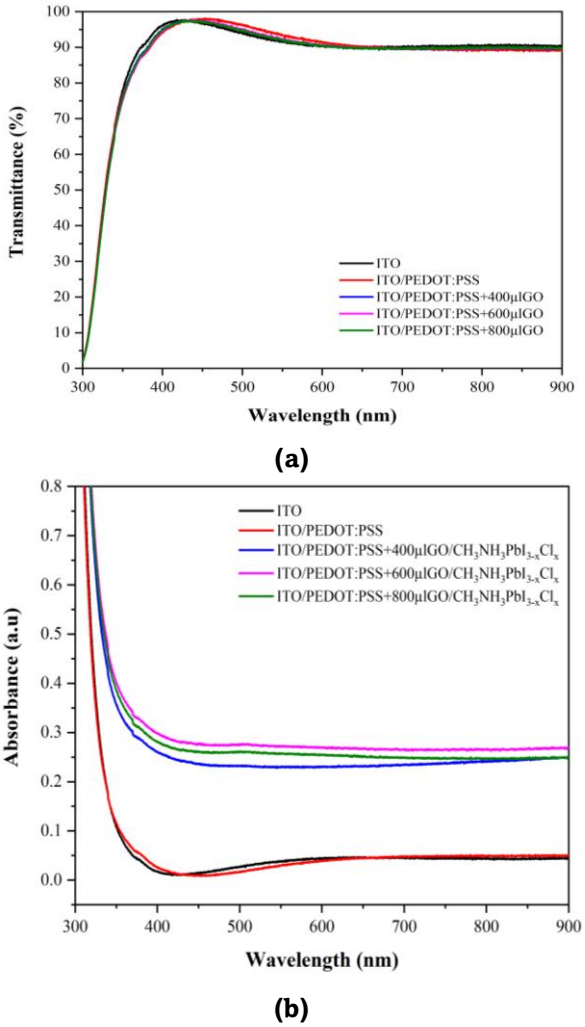

Fig. 3 (a) Transmittance Spectra of ITO and ITO/HTM (b) Absorbance Spectra of ITO, ITO/PEDOT:PSS, and ITO/HTMs/$CH_3NH_3PbI_{3-x}Cl_x$

the perovskite layer. This is driven by GO dispersion properties, which are similar to graphene, which has an optical transparency of up to 97.7% (Khalil, 2019). The perovskite layer plays an important role in the photon absorption process. When light falls on the PSCs, the perovskite layer will absorb light to produce excitons, then charge (electrons and holes) will result from the dissociation of excitons (Hussain *et al.*, 2018). A good perovskite layer must have a higher absorbance value. Perovskite layers were deposited on top of different HTMs, then annealed at 100°C for 25 minutes. The absorbance spectra of the device after deposition of the perovskite layer can be seen in Fig. 3b.

Based on the spectra, it can be seen that there was a significant increase in the absorbance values after the addition of the perovskite layer, indicating that the perovskite layer plays an important role in photon absorption. This is because the perovskite has a high optical absorption coefficient (up to $10^4 cm^{-1}$) (Zhou *et al.*, 2018). The amount of doped GO in PEDOT:PSS as HTM is known to affect the absorbance of the resulting devices. The device with 600 µl GO-doped PEDOT:PSS had the highest absorbance value, followed by the devices with 800 µl and 400 µl doped GO.

The optical response of the fabricated samples was evaluated using UV–Vis spectroscopy to compare the absorption behavior of PSC structures with different GO

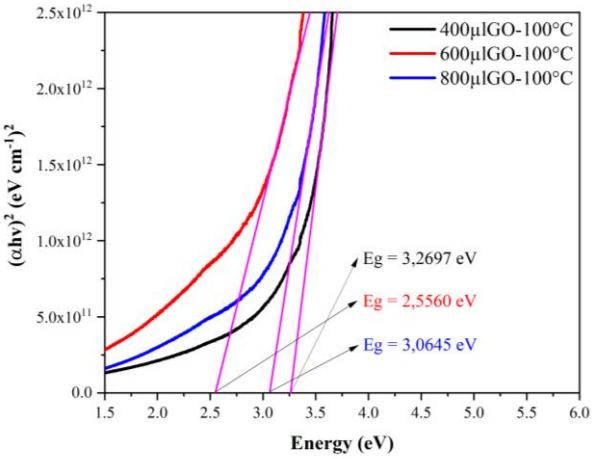

Fig. 4 Tauc plots in the direct-allowed form $(\alpha hv)^2$ versus photon energy (hv) for multilayer PSC stacks with different GO loadings (400, 600, and 800 µL GO in PEDOT:PSS) at 100 °C annealing.

loadings in PEDOT:PSS. The measured spectra correspond to the multilayer configuration (ITO/HTL/$CH_3NH_3PbI_{3-x}Cl_x$-based stack), and therefore include combined optical contributions from the substrate, HTL (including GO), and perovskite-related layers. Accordingly, the optical analysis in this section is used primarily for relative comparison among samples, rather than for extracting the intrinsic bandgap of the perovskite absorber.

For consistency, the optical transition values were estimated using a Tauc plot in the direct-allowed representation, i.e., $(\alpha hv)^2$ versus hv (Tauc & Menth, 1972). However, because the spectra were obtained from a multilayer stack rather than a perovskite-only film, the extrapolated values are treated here as apparent optical transition energies (E_{app}) of the stack, not as the intrinsic bandgap of $CH_3NH_3PbI_{3-x}Cl_x$. The extracted E_{app} values for the GO-loaded samples annealed at 100 °C are approximately 3.2697 eV (400 µL GO), 2.5560 eV (600 µL GO), and 3.0645 eV (800 µL GO), as shown in Fig. 4.

The lower E_{app} observed at 600 µL GO relative to 400 and 800 µL GO indicates a shift in the overall optical response of the stack under the optimum GO-loading condition. Within the limitations of stack-based optical analysis, this shift is interpreted only as a relative indicator of changes in the multilayer optical behavior, which may be influenced by GO-related HTL absorption, interfacial film coverage, and stack morphology. It is not interpreted as a direct change in the intrinsic perovskite bandgap. A rigorous determination of the perovskite bandgap would require optical measurements on a perovskite-only film (with proper baseline/background subtraction and substrate correction), which is beyond the scope of the present dataset.

3.3 Effect of Graphene Oxide Doping on Photoelectric Properties of PSC Devices

All devices were fabricated under ambient laboratory air (25–27 °C; RH ≈ 40%, recorded) without a glovebox to evaluate feasibility under practical, low-temperature processing conditions. Because perovskite crystallization and defect formation are highly sensitive to humidity, processing at ~40% RH can influence grain/void evolution and increase pixel-to-pixel variation unless the recipe is specifically optimized for humid environments. This practical constraint is therefore expected to contribute to the modest JSC/FF observed in this

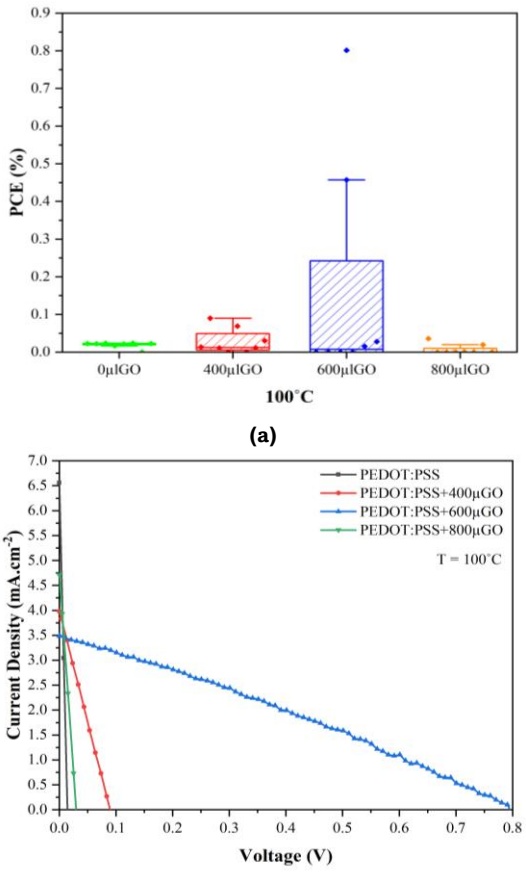

Fig. 5 (a) Effect of GO-Doped PEDOT:PSS on PCE of PSCs, and **(b)** I-V Curve of PSCs with Different HTM.

sustainability-driven proof-of-concept, and it motivates reporting device statistics and resistive metrics (e.g., Rs/Rsh) alongside mean photovoltaic parameters.

The characterization of the solar cell IV test system was carried out to determine the power conversion efficiency (PCE) of PSCs as a function of the addition of doped GO on PEDOT:PSS as HTM. Fig. 5a and 5b respectively show the distribution of PCE values and I-V curves of PSCs with variations of amounts of doped GO (400 µl, 600 µl, and 800µl/1ml PEDOT:PSS) on PEDOT:PSS. For clarity, the GO additions of 400, 600, and 800 µL correspond to 0.4, 0.6, and 0.8 mg GO per 1 mL PEDOT:PSS (equivalent to 0.286, 0.375, and 0.444 mg mL^{-1} in the final mixtures, respectively; approximately 3.1–4.0, 4.6–6.0, and 6.2–8.0 wt% relative to PEDOT:PSS solids). The measurement was carried out on 8 pixels in each sample of PSC, assuming an illumination intensity of 100 mW/cm^2. To assess reproducibility, the photovoltaic parameters are reported as mean ± standard deviation (SD) for n = 8 pixels per condition (Table 2). The optimum device is interpreted in the context of the device population rather than as a standalone result.

Based on the diagram in Fig. 5a, the value of power conversion efficiency (PCE) of PSCs increases with the increase in the amount of doped GO in PEDOT:PSS. The PSC without doped GO produced PCE of 0.0236%, while the highest PCE value was found in the addition of 600 µl GO, which was 0.8011%. The FF and P values also reached the highest value with the addition of 600 µl GO, which were 28.94% and 2.7679 mW, respectively. However, PCE, FF, and P values were observed to decrease with the addition of 800 µl GO. This is due to the poor conductivity of GO due to high oxygen content, so that the use of too much doped GO can reduce the performance of PSCs. According to Wu *et al.* (2014), the lack of conductivity of GO due to its high oxygen content can make the performance of perovskite solar cells very sensitive to the amount of the GO layer (Wu *et al.*, 2014).

To further understand the electrical losses, we measured the series resistance (Rs) and shunt resistance (Rsh) and summarize them in Table 2. A clear trade-off is observed as the GO loading increases. The pristine PEDOT:PSS devices show a

Table 2
Photoelectric properties of Perovskite Solar Cells with Variation of HTM

HTLs	PCE (%)	FF (%)	Jsc ($mA{\cdot}cm^{-2}$)	Voc (V)	P ($mW{\cdot}cm^{-2}$)	Rs ($\Omega{\cdot}cm^2$)	Rsh ($\Omega{\cdot}cm^2$)
PEDOT:PSS	0.0236 ± 0.0071	24.84 ± 2.48	6.5561 ± 0.98	0.0145 ± 0.0058	0.0951 ± 0.0285	150 ± 30	200 ± 80
PEDOT:PSS + 400 µL GO	0.0900 ± 0.0180	25.21 ± 2.02	3.9813 ± 0.56	0.0897 ± 0.0108	0.3571 ± 0.0714	90 ± 18	600 ± 180
PEDOT:PSS + 600 µL GO	0.8011 ± 0.0801	28.94 ± 1.45	3.4825 ± 0.28	0.7948 ± 0.0397	2.7679 ± 0.2214	50 ± 8	1500 ± 300
PEDOT:PSS + 800 µL GO	0.0356 ± 0.0089	25.41 ± 2.03	4.7096 ± 0.66	0.0297 ± 0.0074	0.1399 ± 0.0350	120 ± 24	400 ± 120

high Rs (150 Ω·cm²) and a low Rsh (200 Ω·cm²), which indicates strong resistive loss and large leakage current; this is consistent with the very low Voc and poor FF in the baseline devices. After adding 400 µL GO, Rs decreases to 90 Ω·cm² and Rsh increases to 600 Ω·cm², meaning the current flow becomes easier and leakage is reduced, in line with the higher Voc and improved PCE. The best condition is 600 µL GO, where Rs reaches its minimum (50 Ω·cm²) and Rsh reaches its maximum (1500 Ω·cm²). This explains why FF and PCE are highest at this composition: lower Rs supports a higher FF, and higher Rsh reduces leakage and helps maintain Voc. When GO is increased further to 800 µL, Rs increases again to 120 Ω·cm² and Rsh drops to 400 Ω·cm². This indicates that too much GO makes the HTL more resistive and increases leakage paths, which explains the decrease in FF and PCE. Overall, the Rs/Rsh trend supports an optimum GO loading window and is consistent with the lower conductivity of oxygen-rich GO and potential non-uniform HTL/perovskite coverage at excessive GO content.

We emphasize that the absolute performance values reported here should not be interpreted as technologically competitive. The low FF and modest JSC indicate significant resistive and leakage losses, which are quantitatively supported by the extracted Rs/Rsh trends and are consistent with the SEM-based coverage analysis reported later. In addition, devices were fabricated and measured under ambient air (25–27 °C; RH ≈ 40%, recorded) without glovebox control or encapsulation, which is known to increase defect density and device-to-device variability. Therefore, the primary scientific value of the present dataset lies in demonstrating the feasibility of waste-derived GO as a functional HTL modifier and identifying a clear processing window (moderate GO loading) under practical conditions, rather than in achieving high PCE. In the absence of direct interfacial diagnostics (e.g., EIS, UPS/KPFM, and contact-angle measurements), the observed electrical improvements are interpreted as trends consistent with reduced leakage and resistive losses, rather than as direct proof of recombination suppression or energy-level shifts.

The thickness of the GO-doped PEDOT:PSS HTL was not directly measured in this study and is recognized as a limitation. Since GO addition may change the thickness of the spin-coated HTL and affect resistance and optical transmission, part of the electrical trend may also be influenced by thickness variation. Therefore, the present discussion is limited to trends supported by Rs/Rsh, device statistics, and SEM/XRD observations, while direct HTL thickness measurements will be included in future work.

3.4 Effect of Perovskite Layer Annealing Temperature on Photoelectric Properties of PSC Devices

According to Yu *et al.* (2018), doped GO on PEDOT:PSS can increase the crystallinity of the perovskite layer because perovskite crystals tend to grow more easily on the GO layer than on PEDOT:PSS (Yu *et al.*, 2018). The Perovskite crystal growth is also influenced by the annealing temperature; therefore, the annealing temperature of the perovskite layer can affect the PCE of the fabricated PSCs. The PSCs with 600 µl GO-doped PEDOT:PSS as HTM (the most optimal GO amount) were annealed at varying temperatures of 70°C, 100°C, and 130°C. Photoelectric properties and I-V curves of these are presented in Table 3 and Fig. 6b, respectively. For statistical consistency with the GO-loading analysis, the photovoltaic parameters at each annealing temperature are also reported as mean ± SD for n = 8 pixels (Table 3). These statistics are used to evaluate reproducibility and to avoid over-interpreting single-device values.

Fig. 6a represents the effect of the annealing temperature of the perovskite layer on the PCE of PSCs. Based on the diagram, the PCE value increases with increasing annealing temperature and reaches an optimal value at a

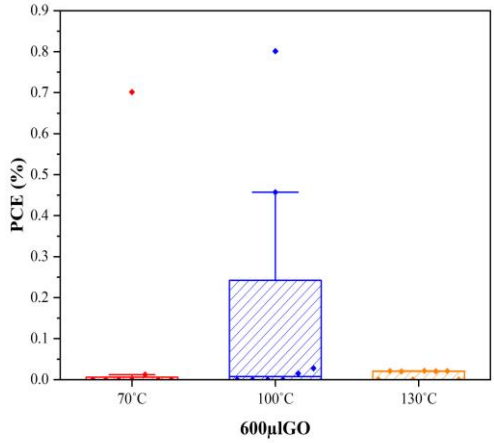

(a)

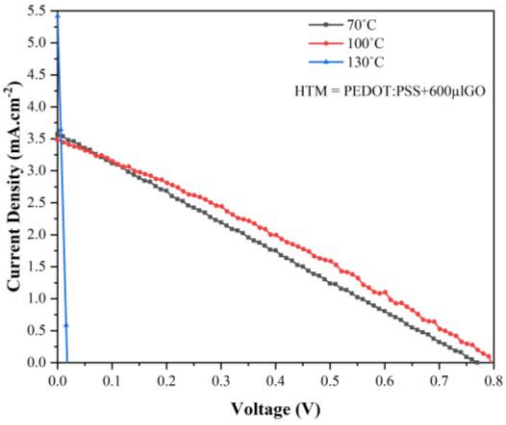

b)

Fig. 6 (a) Effect of Perovskite Layer Annealing Temperature on Power Conversion Efficiency of PSCs, and **(b)** I-V Curve of PSCs with Variation of Perovskite Layer Annealing Temperature

Table 3
Photoelectric Properties of PSCs with Variation of Perovskite Layer Annealing Temperature

Annealing Temperature	PCE (%)	FF (%)	Jsc (mA·cm⁻²)	Voc (V)	P (mW·cm⁻²)	Rs (Ω·cm²)	Rsh (Ω·cm²
70 °C	0.7016 ± 0.1052	25.49 ± 2.04	3.5760 ± 0.36	0.7698 ± 0.0539	2.7528 ± 0.3028	70 ± 11	900 ± 225
100 °C	0.8011 ± 0.0801	28.94 ± 1.45	3.4825 ± 0.28	0.7948 ± 0.0397	2.7679 ± 0.2214	45 ± 7	1500 ± 300
130 °C	0.0213 ± 0.0107	22.04 ± 3.31	5.4198 ± 1.08	0.0178 ± 0.0089	0.0965 ± 0.0483	200 ± 50	80 ± 32

temperature of 100°C. It means that perovskite crystals have formed well at this temperature. Photoelectric properties such as FF and P also have the highest values at that temperature. The PCE, FF, and P values of PSCs with an annealing temperature of 100°C are 0.8011%, 28.94%, and 2.7679 mW. Then, the PCE, FF, and P values decreased at an annealing temperature of 130°C. This decrease in performance is probably caused by damage to the perovskite crystals due to high temperatures.

To quantify resistive and leakage losses associated with annealing, we determined the series resistance (Rs) and shunt resistance (Rsh) and summarize them in Table 3. At 70°C, Rs is 70 Ω·cm² and Rsh is 900 Ω·cm², indicating moderate resistive and leakage losses, which is consistent with incomplete conversion or suboptimal crystallization at low annealing temperature. At the optimum 100°C, Rs decreases to 45 Ω·cm² and Rsh increases to 1500 Ω·cm², meaning current flow is easier and leakage is suppressed; this explains the improvement in FF and the highest PCE at this temperature. In contrast, at 130°C, Rs increases dramatically to 200 Ω·cm² and Rsh drops to 80 Ω·cm², indicating severe shunting/leakage and strong resistive limitations. This strong deterioration in Rs/Rsh provides a clear electrical explanation for the collapse of Voc and the very low PCE at 130°C, and it is consistent with perovskite degradation (PbI_2 formation) under excessive annealing.

3.5 XRD and SEM Characterization of Perovskite Layer Film

The microstructure of the perovskite layer was investigated by X-ray diffraction (XRD). The XRD pattern will determine whether the sample is a single phase or a mixed phase, and impurities (Oku, 2015). In this study, the perovskite layer ($CH_3NH_3PbI_{3-x}Cl_x$) was deposited on top of the ITO/PEDOT:PSS+600µl layer using a spin coating at a speed of 4000 rpm for 30 seconds, then annealed at various temperatures. The XRD pattern of the $CH_3NH_3PbI_{3-x}Cl_x$ layer with various annealing temperatures is presented in Fig. 7.

It is known that there is more than one phase detected in the XRD pattern. The XRD pattern displays diffraction peaks at values of 2θ around 14.48°, 28.70°, 31.70°, and 43.50°, which correspond to the (110), (220), (114), and (330) lattice planes on

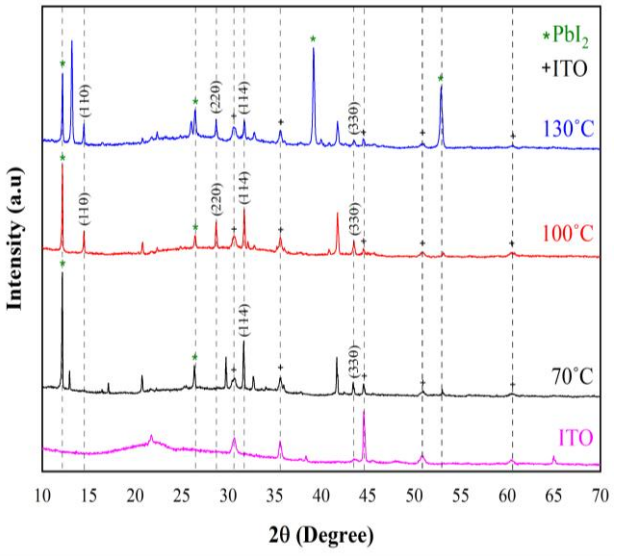

Fig. 7 XRD Pattern of $CH_3NH_3PbI_{3-x}Cl_x$ Layer with Variation of Annealing Temperature: 70°C, 100°C, and 130°C

the $CH_3NH_3PbI_{3-x}Cl_x$ tetragonal crystal. The lattice parameters corresponding to this value are a = 8.800 Å and c = 12.6785 Å (Oku, 2015). Through calculations using the Bragg equation, the d_{hkl} values for the four lattice planes are respectively 6.10939 Å, 3.107257 Å, 2.819925 Å, and 2.078497 Å. Several peaks that appear in the XRD pattern are known to represent PbI_2 (at 2θ around 12.17°), ITO, as well as impurities.

The peak intensity of PbI_2 at 2θ around 12.17° tends to be higher at an annealing temperature of 70°C, then decreases with increasing temperature. The peaks of (110) and (220) planes of $CH_3NH_3PbI_{3-x}Cl_x$ are also not well-formed at this temperature. At an annealing temperature of 100°C, the PbI_2 peak began to decrease, while the (110) and (220) peaks began to form. This indicates that the degree of crystallization increases due to the increase in annealing temperature, and the crystals of $CH_3NH_3PbI_{3-x}Cl_x$ grew well at 100°C. At 130°C, degradation of perovskite to PbI_2 occurred, which was indicated by a decrease in the intensity of the $CH_3NH_3PbI_{3-x}Cl_x$ diffraction peak, as well as the formation of several new peaks representing the XRD pattern of PbI_2 (Bahtiar *et al.*, 2017). Several other unidentified peaks that may be impurities also formed. These peaks are found at 2θ around 13.20° at an annealing temperature of 130°C and about 41.67° at an annealing temperature of 70°C, 100°C, and 130°C. The crystallite size of the perovskite layer can be seen through the peaks of the XRD pattern. In samples consisting of nanoparticles or nanocrystals, the crystal size can be estimated with the full width at half maximum (FWHM) value (Bahtiar *et al.*, 2017). Through calculations using the Scherrer equation, the crystallite size of perovskite is known to vary depending on the annealing temperature used. The average crystallite size of the perovskite layer with an annealing temperature of 70°C is 32.01 nm. This crystallite size increased at 100°C, which was 191.73 nm, and decreased at 130°C, which was 23.69 nm.

The SEM images further provide information about the morphological evolution of the $CH_3NH_3PbI_{3-x}Cl_x$ layer as a result of variations in annealing temperature. In Fig. 8, all samples present the appearance of gray grains and darker parts. The gray granules represent the $CH_3NH_3PbI_{3-x}Cl_x$ layer, while the dark-colored part is the ITO/PEDOT:PSS+600µlGO layer. SEM images showed that the perovskite layer with an annealing temperature of 100°C grew better than that of 70°C. However, some new species were formed and appeared in the $CH_3NH_3PbI_{3-x}Cl_x$ layer annealed at 130°C, which exhibits a relatively brighter contrast compared to the perovskite grains and layers below. This newly formed species has been confirmed in previous studies by Shan *et al.* (2019) that the species is PbI_2 (Shan *et al.*, 2019). This is consistent with the XRD pattern of the perovskite layer, which shows the presence of a PbI_2 component, as discussed in the previous subsection.

The difference in the annealing temperature of the perovskite layer causes differences in the shape and grain size of the perovskite microstructure. At an annealing temperature of 70°C, the microstructure of perovskite has a rounded grain shape, while at 100°C, the grain shape of perovskite is sub-angular. The average grain sizes for the samples prepared with annealing temperatures of 70°C, 100°C, and 130°C were 7.105 µm, 12.045 µm, and 1.568 µm, respectively. In Fig. 8, it can be seen that the perovskite layer has not completely covered all the layers below it. This is indicated by a dark area that is still quite large. The results of the analysis using ImageJ software showed that the percentage of coverage (% coverage) of the perovskite layer was different for each annealing temperature used. The effect of annealing temperature on the % coverage of the perovskite layer is represented in Table 4.

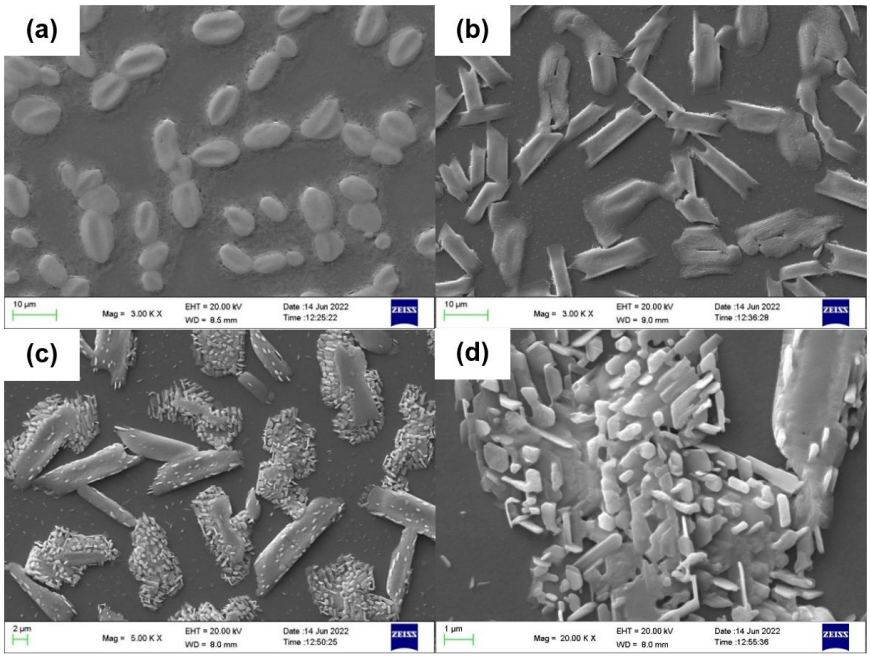

Fig. 8 SEM Images of Perovskite Layer with Annealing Temperature **(a)** 70°C 5000x, **(b)** 100°C 5000x, **(c)**130°C 5000x, and **(d)**130°C 20000x

Table 4
Effect of Annealing Temperature on Percent Coverage of Perovskite Layer

Annealing Temperature	% Coverage			
	Magnification			Average
	1000x	3000x	5000x	
70°C	36.57	37.18	37.07	36.94
100°C	44.8	44.38	43.92	44.36
130°C	41.2	43.92	42.36	42.49

The interfacial interpretation in this work should be considered within the limits of the available measurements. EIS, UPS/KPFM (or Kelvin probe), and contact-angle measurements were not performed; therefore, claims on recombination, energy-level alignment, and wettability are not treated as direct proof but as trends consistent with SEM/XRD observations and Rs/Rsh-based electrical analysis. In addition, fabrication under ambient air (25–27 °C; RH ≈ 40%, recorded) without glovebox optimization likely contributed to the modest absolute PCE and device variability. For this reason, the study is positioned as a circular-materials and process-feasibility proof-of-concept. Future work will include direct interfacial diagnostics and controlled-atmosphere optimization.

4. Conclusion

This work demonstrates a circular-materials route in which electric-arc-furnace graphite-electrode waste is upcycled into graphene oxide (GO) and used to modify PEDOT:PSS as the hole-transport layer in inverted perovskite solar cells. The key finding is that co-optimizing GO loading and a mild perovskite annealing window is critical to device behavior under practical ambient-air processing: moderate GO loading and annealing near ~100 °C produce the best performance among the tested conditions, while excessive GO loading and over-annealing (≈130 °C) lead to increased resistive/leakage losses and strong performance degradation with PbI_2 signatures. The extracted Rs/Rsh trends, together with SEM/XRD observations, provide a quantitative basis for identifying this processing window under the tested conditions. Although the absolute efficiency remains modest, the study validates waste-derived GO as a functional HTL modifier and establishes a sustainability-driven proof-of-concept linking metallurgical by-products to photovoltaic interface engineering. Future work will focus on controlled-atmosphere process optimization and direct interfacial diagnostics (EIS, UPS/KPFM, and contact-angle measurements) to validate the interfacial mechanisms and improve absolute device performance.

Acknowledgments

The authors gratefully acknowledge the financial support from the Ministry of Higher Education, Science, and Technology of the Republic of Indonesia (Kemendiktisaintek) under the Research Grant of Program Hilirisasi Riset Prioritas - Sinergi No. 258/SPK/C.C4/PPK.DHK/IX/2025. This sponsorship

provided the framework and resources necessary to conduct the present study. The authors also acknowledge the use of facilities at the Integrated Laboratory (Laboratorium Terpadu), Universitas Sultan Ageng Tirtayasa, which supported material synthesis and characterization throughout this work.

Author Contributions: Y.R.D., M.F.: Conceptualization, methodology, formal analysis, writing—original draft, Y.R.D.; supervision, resources, project administration, M.I.S., S.D.R., R.J., M.; writing—review and editing, validation. All authors have read and agreed to the published version of the manuscript.

Funding: The Ministry of Higher Education, Science, and Technology of the Republic of Indonesia (Kemendiktisaintek) under the Research Grant of Program Hilirisasi Riset Prioritas - Sinergi No. 258/SPK/C.C4/PPK.DHK/IX/2025

Conflicts of Interest: (state the conflicts of interest, if any) or if not: The authors declare no conflict of interest.

References

Al-Gamal, A. G., Elseman, A. M., Abdel-Shakour, M., Chowdhury, T. H., Kabel, K. I., Farag, A. A., Rabie, A. M., El-Sattar, N. E. A. A., Fukata, N., & Islam, A. (2023). Synergistic effect of integrating N-functionalized graphene and PEDOT:PSS as hole transporter bilayer for high-performance perovskite solar cells. *Advanced Composites and Hybrid Materials*, *6*(3), 103. https://doi.org/10.1007/s42114-023-00681-w

Ali, I., Faraz Ud Din, M., Cuzzupè, D. T., Fakharuddin, A., Louis, H., Nabi, G., & Gu, Z.-G. (2022). Ti3C2Tx-Modified PEDOT:PSS Hole-Transport Layer for Inverted Perovskite Solar Cells. *Molecules*, *27*(21), 7452. https://doi.org/10.3390/molecules27217452

Al-Mousoi, A. K., Mehde, M. S., & Al-Gebori, A. M. (2020). Annealing temperature effects on the performance of the perovskite solar cells. *IOP Conference Series: Materials Science and Engineering*, *757*(1), 012039. https://doi.org/10.1088/1757-899X/757/1/012039

Bahtiar, A., Rahmanita, S., & Inayatie, Y. D. (2017). Pin-Hole Free Perovskite Film for Solar Cells Application Prepared by Controlled Two-Step Spin-Coating Method. *IOP Conference Series: Materials Science and Engineering*, *196*(1), 012037. https://doi.org/10.1088/1757-899X/196/1/012037

Eluyemi, M. S., Eleruja, M. A., Adedeji, A. V., Olofinjana, B., Fasakin, O., Akinwunmi, O. O., Ilori, O. O., Famojuro, A. T., Ayinde, S. A., & Ajayi, E. O. B. (2016). Synthesis and Characterization of Graphene Oxide and Reduced Graphene Oxide Thin Films Deposited by Spray Pyrolysis Method. *Graphene*, *5*(3), 143–154. https://doi.org/10.4236/graphene.2016.53012

Er-raji, O., Rustam, L., Kore, B. P., Glunz, S. W., & Schulze, P. S. C. (2023). Insights into Perovskite Film Formation Using the Hybrid Evaporation/Spin-Coating Route: An In Situ XRD Study. *ACS Applied Energy Materials*, *6*(11), 6183–6193. https://doi.org/10.1021/acsaem.3c00698

Garg, K. K., Pandey, S., Pathak, M., Sharma, C. P., Kumar, A., Pandey, L., Arnusch, C. J., Sahoo, N. G., Dhawan, S. K., Lee, M.-J., & Singh, R. K. (2024). Mass scale synthesis of graphene nanosheets using waste cardboard for application in perovskite solar cells and supercapacitors. *Heliyon*, *10*(9). https://doi.org/10.1016/j.heliyon.2024.e30263

Han, W., Ren, G., Liu, J., Li, Z., Bao, H., Liu, C., & Guo, W. (2020). Recent Progress of Inverted Perovskite Solar Cells with a Modified PEDOT:PSS Hole Transport Layer. *ACS Applied Materials & Interfaces*, *12*(44), 49297–49322. https://doi.org/10.1021/acsami.0c13576

Hussain, I., Tran, H. P., Jaksik, J., Moore, J., Islam, N., & Uddin, M. J. (2018). Functional materials, device architecture, and flexibility of perovskite solar cell. *Emergent Materials*, *1*(3), 133–154. https://doi.org/10.1007/s42247-018-0013-1

Insiyanda, D. R., Widodo, H., Khaerudini, D. S., Gumilar, D. A., Chanif, I., & Indayaningsih, N. (2019). Preparation of Graphite Electrode Waste/Natural Carbon Black/Polyvinylidene Fluoride Composites Using Liquid Nitrogen Cold Quenching. *Journal of Physics: Conference Series*, *1191*(1), 012063. https://doi.org/10.1088/1742-6596/1191/1/012063

Johra, F. T., Lee, J.-W., & Jung, W.-G. (2014). Facile and safe graphene preparation on solution based platform. *Journal of Industrial and Engineering Chemistry*, *20*(5), 2883–2887. https://doi.org/10.1016/j.jiec.2013.11.022

Khalil, E. K., Atik Suhrowati, Anwar Usman, Volkan Degirmenci, Munawar. (2019). Synthesis and Characterization of Graphite Oxide, Graphene Oxide and Reduced Graphene Oxide from Graphite Waste using Modified Hummers's Method and Zinc as Reducing Agent. *IJTech - International Journal of Technology*. 10(6), 1093-1104. https://doi.org/10.14716/ijtech.v10i6.3639

Luo, H., Lin, X., Hou, X., Pan, L., Huang, S., & Chen, X. (2017). Efficient and Air-Stable Planar Perovskite Solar Cells Formed on Graphene-Oxide-Modified PEDOT:PSS Hole Transport Layer. *Nano-Micro Letters*, *9*(4), 39. https://doi.org/10.1007/s40820-017-0140-x

Mateen, M., Li, Z., Shi, H., Huang, H., Khan, D., Khan, R. A. A., Rafiq, M., Syed, J. A. S., Khaliq, A., Ashraf, G. A., Tsiba, J. M., Lu, Z., Chi, D., & Huang, S. (2023). Engineering the intermediate adduct phase to control the crystallization of perovskites for efficient and stable perovskite solar cells. *Materials Chemistry Frontiers*, *7*(18), 4080–4091. https://doi.org/10.1039/D3QM00537B

Nguyen, D. C. T., Mai, V.-D., Tran, V.-H., Vu, V.-P., & Lee, S.-H. (2022). Use of modified PEDOT:PSS/Graphene oxide dispersions as a hole transport layer for inverted bulk-heterojunction organic solar cells. *Organic Electronics*, *100*, 106388. https://doi.org/10.1016/j.orgel.2021.106388

Niu, J., Yang, D., Ren, X., Yang, Z., Liu, Y., Zhu, X., Zhao, W., & Liu, S. (Frank). (2017). Graphene-oxide doped PEDOT:PSS as a superior hole transport material for high-efficiency perovskite solar cell. *Organic Electronics*, *48*, 165–171. https://doi.org/10.1016/j.orgel.2017.05.044

Oku, T. (2015). Crystal Structures of CH3NH3PbI3 and Related Perovskite Compounds Used for Solar Cells. In *Solar Cells—New Approaches and Reviews*. IntechOpen. https://doi.org/10.5772/59284

Sadeli, Y., Soedarsono, J. W., Prihandoko, B., & Harjanto, S. (2011). Study on Graphite Electric Arc Furnace Waste as a Bipolar Plate Composite Material for Polymer Electrolyte Membrane Fuel Cell (PEMFC) Application. *Journal of Materials Science and Engineering. B*, *1*(2B), 178.

Shan, D., Tong, G., Cao, Y., Tang, M., Xu, J., Yu, L., & Chen, K. (2019). The Effect of Decomposed PbI2 on Microscopic Mechanisms of Scattering in CH3NH3PbI3 Films. *Nanoscale Research Letters*, *14*(1), 208. https://doi.org/10.1186/s11671-019-3022-y

Tauc, J., & Menth, A. (1972). States in the gap. *Journal of Non-Crystalline Solids*, *8–10*, 569–585. https://doi.org/10.1016/0022-3093(72)90194-9

Wargulski, D. R., Xu, K., Hempel, H., Flatken, M. A., Albrecht, S., & Abou-Ras, D. (2023). Relationship between the Annealing Temperature and the Presence of PbI2 Platelets at the Surfaces of Slot-Die-Coated Triple-Halide Perovskite Thin Films. *ACS Applied Materials & Interfaces*, *15*(35), 41516–41524. https://doi.org/10.1021/acsami.3c07692

Wazir, A. H., & Kundi, I. W. (2016). Synthesis of Graphene Nano Sheets by the Rapid Reduction of Electrochemically Exfoliated Graphene Oxide Induced by Microwaves. *Journal of the Chemical Society of Pakistan*. *38*(1), 11–16.

Wu, Z., Bai, S., Xiang, J., Yuan, Z., Yang, Y., Cui, W., Gao, X., Liu, Z., Jin, Y., & Sun, B. (2014). Efficient planar heterojunction perovskite solar cells employing graphene oxide as hole conductor. *Nanoscale*, *6*(18), 10505–10510. https://doi.org/10.1039/C4NR03181D

Yang, J., Luo, X., Zhou, Y., Li, Y., Qiu, Q., & Xie, T. (2022). Recent Advances in Inverted Perovskite Solar Cells: Designing and Fabrication. *International Journal of Molecular Sciences*, *23*(19), 11792. https://doi.org/10.3390/ijms231911792

Yu, J. C., Hong, J. A., Jung, E. D., Kim, D. B., Baek, S.-M., Lee, S., Cho, S., Park, S. S., Choi, K. J., & Song, M. H. (2018). Highly efficient

and stable inverted perovskite solar cell employing PEDOT:GO composite layer as a hole transport layer. *Scientific Reports*, *8*(1), 1070. https://doi.org/10.1038/s41598-018-19612-7

Zhou, D., Zhou, T., Tian, Y., Zhu, X., & Tu, Y. (2018). Perovskite-Based Solar Cells: Materials, Methods, and Future Perspectives. *Journal of Nanomaterials*, *2018*(1), 8148072. https://doi.org/10.1155/2018/8148072

© 2026. The Author(s). This article is an open access article distributed under the terms and conditions of the Creative Commons Attribution-ShareAlike 4.0 (CC BY-SA) International License (http://creativecommons.org/licenses/by-sa/4.0/)